Materials Science & Engineering A 788 (2020) 139608

Contents lists available at ScienceDirect

Materials Science & Engineering A

journal homepage: http://www.elsevier.com/locate/msea

The effect of loading direction on strain localisation in wire arc additively manufactured Ti–6Al–4V

David Lunt [a,*], Alistair Ho [a], Alec Davis [a], Allan Harte [a,c], Filomeno Martina [b], João Quinta da Fonseca [a], Philip Prangnell [a]

[a] University of Manchester, Oxford Road, Manchester, M13 9PL, UK
[b] Welding Engineering and Laser Processing Centre, Cranfield University, Bedfordshire, MK43 0AL, UK
[c] United Kingdom Atomic Energy Authority, Culham Science Centre, Abingdon, OX14 3DB, UK

ARTICLE INFO

Keywords:
Titanium alloys
Additive manufacturing
Tensile
EBSD
Digital image correlation
Strain localisation

ABSTRACT

Ti–6Al–4V microstructures produced by high deposition rate Wire Arc Additive Manufacturing (WAAM) can be both heterogeneous and anisotropic. Key features of the as-built microstructures include; large columnar ß grains, an α transformation texture inherited from the β solidification texture, grain boundary (GB) α colonies, and Heat Affected Zone (HAZ) banding. The effect of this heterogeneity on the local strain distribution has been investigated using Digital Image Correlation (DIC) in samples loaded in tension; parallel (WD), perpendicular (ND) and at 45° (45ND) to the deposited layers. Full-field surface strain maps were correlated to the underlying local texture. It is shown that loading perpendicular to the columnar β grains leads to a diffuse heterogeneous deformation distribution, due to the presence of regions containing hard, and soft, α microtextures within different parent β grains. The 'soft' regions correlated to multi-variant α colonies that did *not* contain a hard α variant unfavourably orientated for basal or prismatic slip. Far more severe strain localisation was seen in 45° ND loading at 'soft' β grain boundaries, where single variant α GB colonies favourably orientated for slip had developed during transformation. In comparison, when loaded parallel to the columnar ß grains, the strain distribution was relatively homogeneous and the HAZ bands did not show any obvious influence on strain localisation at the deposit layer-scale. However, when using high-resolution DIC, as well as more intense shear bands being resolved at the β grain boundaries during 45° ND loading, microscale strain localisation was observed in HAZ bands below the yield point within the thin white-etching α colony layer.

1. Introduction

Titanium alloys (and Ti–6Al–4V in particular) are extensively used in the aerospace industry due to their excellent combination of properties, which include high specific strength, good corrosion resistance and high damage tolerance, but suffer from high processing and manufacturing costs [1–4]. Recent developments in Additive Manufacturing (AM) have the potential to enable the production of near-net shape parts with shorter lead times and greater design flexibility [5–12]. Several wire-fed Direct Energy Deposition (DED) AM technologies are currently being investigated for producing larger-scale components [13] which have the advantage, compared to powder bed systems, of much higher deposition rates (e.g. 4–10 kg/hr), but the disadvantage of lower layer resolution and part complexity [10,11,14]. The larger melt pool and layer height inherent to higher deposition rate processes also leads to lower cooling rates and greater microstructure heterogeneity [14]. In this study, the Wire-Arc Additive Manufacturing (WAAM) process was investigated, which uses an electric (plasma) arc as its heat source and is capable of reaching deposition rates greater than 4 kg/h [15].

It is now widely acknowledged that DED-AM process with Ti–6Al–4V can give rise to specific types of macroscale microstructural heterogeneity, not normally seen in wrought products [8,16–19]. A common feature of DED-AM with Ti–6Al–4V is the formation of coarse-columnar parent β grains that can span millimetres in length and are oriented close to the build direction, with an $<001>_{BCC}$ fibre solidification texture [20–28]. On cooling of each deposited layer, this solidification structure can lead to local texture and microstructure variation in the transformed lamellar α, owing to the Burgers Orientation Relationship (BOR) [29] and the tendency for grain boundary (GB) nucleation. This includes the presence of α allotriomorphs on the β GBs and an associated single

* Corresponding author.
E-mail address: david.lunt@manchester.ac.uk (D. Lunt).

https://doi.org/10.1016/j.msea.2020.139608
Received 20 March 2020; Received in revised form 16 May 2020; Accepted 18 May 2020
Available online 21 May 2020

variant 'colony' α GB layer, along with multi-variant α colonies forming in the matrix (the so-called basket weave microstructure) [30] that have a restricted set of variant orientations (typically three) related by the BOR to their parent β grain. Furthermore, the high temperature gradients and multiple thermal cycles experienced during deposition can lead to additional microstructural variation [19,21,23–27,31–34]. With sequential deposition passes in AM, each layer experiences a complex cyclic thermal history that can result in systematic variation in the local microstructural parameters. In particular, heat affected zone (HAZ) 'bands', with a regular spacing equivalent to the layer height, are commonly observed in wire-based AM processes [19,21,23–27,31–34]. The microstructure divergence in the HAZ band regions results from re-heating to temperatures below the β transus, but within the β approach curve, where substantial coarsening of α can occur [15]. The top of each HAZ band is also typically delineated by a thin white-etching layer consisting of a fine, α - single variant - colony microstructure, which with the WAAM processes is roughly 100–200 μm in width [15].

The formation of such microstructure heterogeneities can potentially lead to unpredictability in the performance of components. Significant anisotropy has been observed in the mechanical behaviour of AM deposits when tested in different loading directions, which is detrimental for applications involving multidirectional stresses [8]. Anisotropy in tensile strength has been linked to the large columnar parent β grain structures exhibiting a preferential crystallographic orientation that influences the α texture [22,35–39], whilst anisotropy in ductility has been attributed to rupture of the soft grain boundary α layer present on the parent ß grain boundaries [20,26,33,34,37,40]. Yang et al. [38] found that, in a selective laser melting (SLM) processed material, the average α Schmid factor was higher for horizontally built than vertically built samples and, in terms of mechanical properties, the horizontally built samples exhibited higher yield strengths, whereas the vertically built samples exhibited better elongation. In high deposition rate DED-laser deposited materials, a difference in ductility with respect to the loading direction has also been attributed to a softer grain boundary α layer being present at parent ß grain boundaries [14]. In this work it has been suggested that when loading perpendicular to the build height, tensile loads are exerted normal to the long axes of the β grains causing the grain boundary α to fail prematurely, which then separates adjacent ß grains.

To shed more light on the relative importance of different sources of microstructure/texture heterogeneity-related strain localisation, in high deposition rate DED-WAAM titanium materials, here Digital Image Correlation (DIC) has been used to compare the strain distribution that develops in static tensile loading (in the as-built condition) in different orientations with respect to the build direction. DIC is a robust experimental method for enabling full-field measurements [41–50] and is an attractive technique for application to multiple length scales, since the method does not possess an inherent scale (i.e. this is dependent on the speckle pattern used) [41]. Full-field displacement maps can be readily produced by tracking suitable features on the surface of a specimen during deformation. For example, Littlewood and Wilkinson [50] and Lunt et al. [51] have shown the benefits of observing differences in strain localisation in heterogeneous Ti–6Al–4V wrought products using optical DIC, with surface patterns generated by Focus Ion Beam (FIB) milling and etched microstructures, respectively. Limited previously published work, using DIC for investigating strain localisation in AM manufactured Ti–6Al–4V, has also indicated that local regions with different microtextures at parent β grain boundaries can play an important role in strain localisation [52]. However, the relatively high-resolution of the strain measurements used meant that only a few β grains were studied and the overall macroscale heterogeneity was not captured.

The aim of the current paper was, therefore, to use a more comprehensive multi-scale approach to study strain localisation in high deposition rate AM samples. This involved first using full-field optical DIC to identify regions of micron-scale strain localisation in the underlying WAAM microstructures, and confirm whether changing the loading direction had a significant impact on the strain patterns developed. By capturing the entire gauge length across 26 mm tensile samples, the macroscopic deformation behaviour was observed, enabling critical regions of high and low strain localisation to be identified, so that they could be subsequently correlated in greater detail to their local microtexture and slip behaviour. This initial study was then supported by selected higher resolution DIC measurements. In WAAM materials, where there is large scale microstructural heterogeneity, this multiscale approach has thus facilitated understanding of the relative influence of the main types of microstructural inhomogeneity (such as HAZ banding, columnar grains or grain boundary α), in terms of their significance to strain localisation, as well as enabling their underlying physical origin to be determined.

2. Experimental methods

2.1. Material - samples

A single deposition pass, wide wall, 55 layers high (250 mm long by 80 mm high, each layer was ~1.4 mm high, by 7 mm thick) was produced by plasma wire deposition (PWD) at Cranfield University Welding Engineering Research Centre UK (2012 F. Martina Plasma deposition). The component was deposited on a Ti–6Al–4V rolled plate substrate using a constant heat source travel direction. The deposition parameters are summarised in Table 1. The sample reference frame used throughout is defined as; WD, the wall and heat source traverse direction; TD, the wall transverse direction and ND the build height, or layer normal, direction. Thin, flat, dog-bone tensile specimens with a 26 mm gauge length, 3 mm width and 1 mm thickness, were used for the optical DIC and High-resolution DIC (HRDIC) experiments. A low sample thickness was used to reduce the effect of through-thickness microstructure/microtexture variation on the DIC surface measurements. The specimens were manufactured using electric discharge machining (EDM) in the plane of the wall at three different orientations, so that their axes were aligned approximately; i) perpendicular to the HAZ bands and deposited layers, ii) at 45° to the deposited layers, and iii) normal to the columnar β grain's long boundaries. These samples have been designated *ND*, *45ND* and *WD*, respectively. It should be noted that, due to the constant heat source travel direction employed, the β grains were tilted by about 15° towards WD, so that the WD sample was tilted by a similar amount from WD. The samples were all machined out of the steady state region of the wall; i.e. from 15 layers above the substrate and below the final HAZ band. One flat surface of each tensile sample was mechanically polished to 4000 grit, followed by hand polishing for 10 min in a colloidal silica suspension (OP–S) mixed with 5% concentrated hydrogen peroxide (H_2O_2). This surface was subsequently etched in Kroll's solution for approximately 3 min, to provide a distinct speckle pattern for DIC. The etchant revealed the α boundaries within the microstructure sufficiently to enable successful optical scale DIC measurements (see Fig. 1).

To study the behaviour of the HAZ bands and a β grain boundary region, where high strain localisation was observed from the 45ND sample at higher resolution, a further set of two samples (one extracted

Table 1
The WAAM-PAW deposition parameters employed in this study.

Wire Feed Speed	2.4 m min^{-1}
Travel Speed	7 mm s^{-1}
1st 6 Layers Current	165 A
Current after 6 layers	150 A
Plasma Gas	1 L min-1
Local Shielding Gas (Argon)	10 L min-1
Trailing Shielding Gas	25 L min-1
Work Piece Distance/Torch stand off	8 mm
Wire Type	Ti–6Al–4V ERTi-5
Wire Specification	1.2 mm * D300

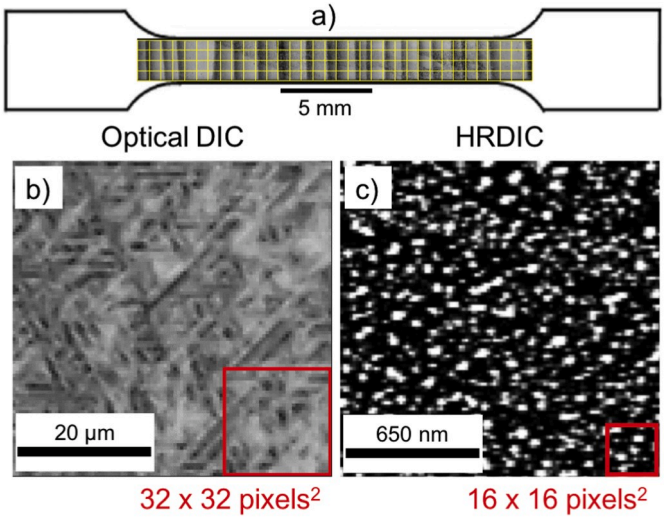

Fig. 1. Examples of the DIC image acquisition process; a) an image tile map superimposed on the entire gauge length of the specimen for the optical DIC and the pattern resolution used; b) in the optical microscope and c) in the SEM for HRDIC. The respective interrogation window sizes are indicated by the red boxes. (For interpretation of the references to colour in this figure legend, the reader is referred to the Web version of this article.)

from the ND and the other from the pre-strained 45ND samples used in the optical DIC analysis) were prepared for HRDIC using the gold remodelling technique detailed in Refs. [53,54]. A pre-strained 45ND sample was used to enable the strain localisation around a heavily deformed parent β grain boundary to be first identified from the optical DIC. To produce gold nano-dot speckle pattern, a thin gold film of ~ 5 nm was deposited on to the surface of the samples using an Edwards S150B sputter coater, at a current of 40 mA for 5 min. The thin film was subsequently remodelled to form distinct gold nano-islands of approximately 40–80 nm in diameter, by heating in an enclosed chamber with a water vapour source at a temperature of 280 °C for 4 h.

2.2. Digital image correlation and mechanical loading

Optical DIC ex-situ tensile loading experiments were performed using a Deben UK Ltd 5 kN tensile/compression microtester, under displacement control at a rate of 0.02 mm/min, to give real-time displacement and load data. The sample displacements were subsequently transformed to engineering strain relative to the initial sample gauge length. The macroscopic sample strains provided below with the DIC strain maps are from the unloaded condition and therefore represent plastic strains, as to obtain the images for DIC analysis samples were removed from the microtester after each deformation step and image mapped using a Zeiss Axio Imager 2 optical microscope, equipped with built-in automated mapping software. 48 points across the surface were first manually selected before performing each map, to ensure accurate focus interpolation. The images taken were 1648 x 1436 pixels^2 in area, at a spatial resolution of 0.547 μm/pixel, and had a 20% overlap. Each matrix of images was 4 frames wide across the gauge width, by at least 36 along the gauge length (Fig. 1a), and were stitched together using ImageJ image processing software prior to DIC analysis. Loading and subsequent imaging was repeated in small increments of ~ 0.5% strain, up to an applied sample strain in the loading direction of ~3–5%. In each imaging step, after unloading, the edges of the samples were aligned parallel to the first imaging condition to minimise any rotation artefacts that may cause issues with the correlation algorithm. In the experiments the samples were not strained to failure to enable post-deformation EBSD and surface slip characterisation of selected areas of interest. The stitched images at different deformation steps were processed using LaVision's DIC software, DaVis version 8.4. The relative local displacements were computed by dividing the image into sub-regions and then determining the relevant strain value by differentiating the appropriate displacements. A standard fast Fourier transform (FFT) was applied with a final interrogation window size of 32 x 32 pixels^2, equating to a spatial resolution of 17.51 × 17.51 μm^2 (Fig. 1b).

The HRDIC measurements were also performed using ex-situ tensile loading experiments with the same microtester and at the same strain rate as for the optical DIC samples. In these experiments the ND sample was deformed to ~80% of the yield strength, i.e. in the 'elastic' region, and the pre-strained 45ND sample was deformed another ~1% plastically, to resolve the GB slip intensity. The images for HRDIC analysis were acquired using a high-resolution FEI Magellan field emission gun scanning electron microscope (FEG-SEM) in back-scattered electron (BSE) imaging mode, using a concentric back-scattered (CBS) detector, at an accelerating voltage of 5 kV and beam current of 0.8 nA. The working distance was approximately 4 mm (to maximise the BSE signal). The horizontal image field width was 30 μm. Each image took ~10 s to record and all images were acquired at a resolution of 2048 x 1768 pixels^2 in a scan mode with a 3 μs dwell time. Arrays of images were automatically recorded using FEI MAPS software, with a 20% overlap, and focus was maintained using a 3-point focus correlation function. The images were again stitched together before DIC processing, using ImageJ, and then analysed using the LaVision software, with a final interrogation window size of 16 x 16 pixels^2, which gave a spatial resolution of 0.23 × 0.23 μm^2.

The optical DIC and HRDIC data is presented below in terms of the effective shear strain, γ_{eff}, to help reduce the ambiguity caused by the lack of out-of-plane information which not accessible from 2D surface DIC [45,51]. This was calculated by the standard relationship:

$$\gamma_{eff} = \sqrt{\left(\frac{(\varepsilon_{xx} - \varepsilon_{yy})}{2}\right)^2 + \left(\frac{(\varepsilon_{xy} + \varepsilon_{yx})}{2}\right)^2} \quad (1)$$

Where ε_{xx} is the strain in the loading direction, ε_{yy} is the strain normal to the loading direction and $\frac{(\varepsilon_{xy}+\varepsilon_{yx})}{2}$ is the in-plane shear component.

2.3. SEM imaging and grain orientation mapping

Post deformation, regions of interest were marked with micro hardness indents and the samples were lightly re-polished with a colloidal silica solution to remove the DIC pattern and allow electron back scatter diffraction (EBSD) analysis to be performed. EBSD maps were produced using a Sirion FEG-SEM equipped with an AZtec EBSD system and a Nordlys II detector, at various step sizes (dependent on the features of interest) and at an accelerating voltage of 20 kV. The EBSD maps were analysed with HKL Channel 5^{TM} software and then aligned with regions of interest observed in the DIC strain maps, so that the orientations of the α variants present and their Schmid factors, for different slip modes, could be correlated to the local deformation behaviour. As it is very difficult to resolve the small volume fraction (~5%) of thin retained β in WAAM materials by EBSD, ß reconstruction software developed by Davies et al. was used to characterize the parent ß grain's morphology and orientation from the room temperature α variants [55]. Images for more detailed microstructural analysis were also taken using an FEI Magellan, and FEI mapping software, operated at 8 kV with a 1.6 nA beam current as described further in Ref. [15].

3. Results and discussion

3.1. WAAM microstructure heterogeneity

In Fig. 2 macroscopic views are depicted from the centre ND-WD plane of an as-built Ti–6Al–4V single bead-wide WAAM wall, to provide examples of the larger-scale microstructure and texture heterogeneity features of interest in this study. It can be seen that the as-

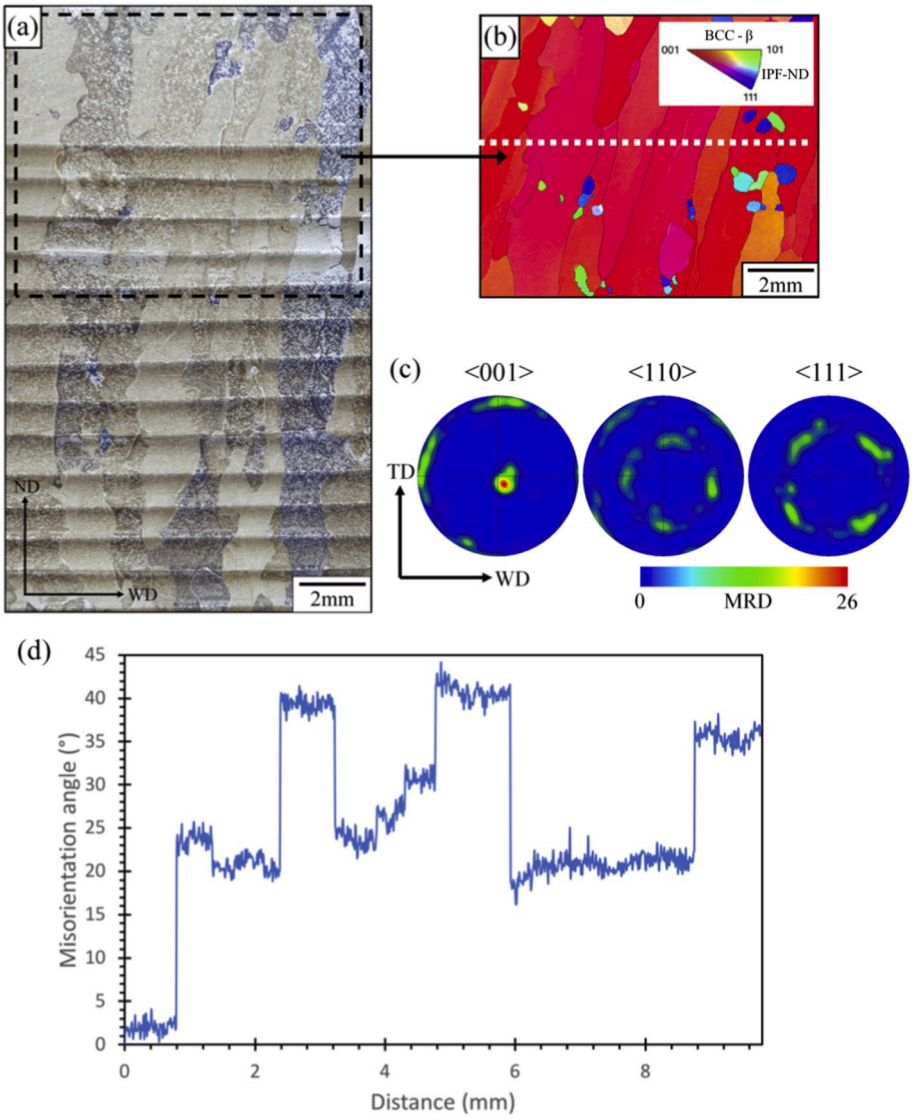

Fig. 2. Examples of the typical heterogeneities of interest seen in an as-built Ti–6Al–4V WAAM wall showing; (a) a section through the centre ND-WD plane up to the top the wall and (b) a reconstructed ß EBSD map with IPF-ND colouring, taken from the area shown in (a), and (c) the corresponding <001>, <110> and <111> β-phase pole figures. (d) Shows a misorientation profile across the ß IPF-ND map, along the dashed line indicated in (b).

deposited wall contains very coarse-columnar β grains, aligned close to ND, with a tilt of ~ 10–15° around TD towards the heat source travel direction (WD). The grains have a common <001> crystallographic growth orientation, which develops during epitaxial solidification over multiple layers and, therefore, appear red in the IPF//ND colouration, reconstructed, EBSD orientation map (Fig. 2b). The corresponding strong β phase <001> fibre texture is shown in the pole figures in Fig. 2c. The misorientation profile shown in Fig. 2d, taken along the white dashed line in the reconstructed ß IPF-ND map (Fig. 2b) indicates that relatively low misorientations of less than 20° are typically found between the neighbouring parent β grains because of their strong texture and common <001> growth direction.

In Fig. 2a horizontal, dark – white etched, HAZ bands can be seen are aligned parallel to the deposited layers [15] with a spacing equivalent to the layer height. The HAZ bands are generated by the moving heat source and appear as a locus of where the peak temperature reached was within the range of the β transus approach curve; i.e. ~ 850–1000 °C [15]. The top region of the wall above the last HAZ band was fully β transformed in the last deposition pass and was not included within the tensile samples. The bottom 15 layers of the build are influenced by the heat sinking from the substrate and were also excluded from the tensile samples. Higher magnification SEM images area also provided in Fig. 3 and Fig. 4, showing important regions of heterogeneity in the transformation microstructure. Fig. 3 depicts a β columnar GB, with an associated layer of single variant colony α growing either side of the boundary into each neighbouring β grain. In Fig. 4a, a graph of the average α lamellae plate spacing, measured across a typical deposition layer encompassing a HAZ band is shown. This is accompanied by example images of; the fine basket weave multi-variant lamellar α microstructure found between the HAZ bands (Fig. 4b), the coarsened basket weave α seen after exposure to higher peak temperatures (~ 900 °C) in the dark etch region of a HAZ band (Fig. 4c), and the finer single-variant α colony microstructure found within the thin 'white etching layer' [15] seen at the top of each HAZ band (Fig. 4d) - formed where the peak temperature reached was very close to the β transus. A full description of how the Ti–6Al–4V microstructure transition develops across a HAZ band in the WAAM process, and how the α lamellae spacing measurements were made, can be found in our previous publication [56]. In these higher resolution images it can be noted that the GB single variant colony α and thin layer of colony α at the top of each HAZ band have some similar features; in that they are dominated by domains comprised of single α variants, with a finer lamellar spacing than seen in

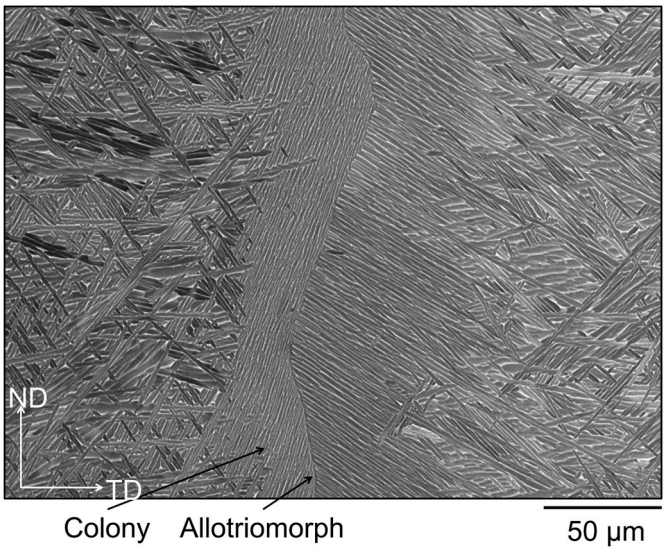

Fig. 3. SEM backscatter electron image of α allotriomorph and colonies growing off a prior columnar beta grain boundary, surrounded by conventional Widmanstätten basket weave microstructure in a typical WAAM component.

the multi-variant basket weave [57] microstructure which comprises the majority of the transformed material found within the matrix of the coarse β grains.

From the above description (Fig. 2), and inspection of Fig. 5 below, it is apparent that the ND DIC samples contained only a few (2–3) columnar grains that were approximately parallel to and extended, along their entire length, but were loaded nearly perpendicular to the orientation of the HAZ bands, which are parallel to the deposited layers. In comparison, the WD samples were orientated approximately normal to the axes of the coarse β grains, which extended fully across their gauge width and depth. The tensile samples used for the DIC experiments thus contained multiple parallel β GBs aligned approximately perpendicular to the tensile axis, when viewed at the samples 2D polished surface, although it should be noted the GB plane could be still inclined through the sample thickness (in TD). In these samples, due to them being machined normal to the β grains major axis, the HAZ bands were tilted by ~ 10–15° relative to the tensile axis in the ND-WD surface used for DIC and extended through the sample thickness normal to the sample surface. Finally, the 45ND sample also contained multiple β grain boundaries as well as HAZ bands orientated at approximately '+' and '-' 45° to the tensile axis, respectively, in the samples' surface plane, which would make both features nearly coincident with the plane of maximum shear stress during tensile loading.

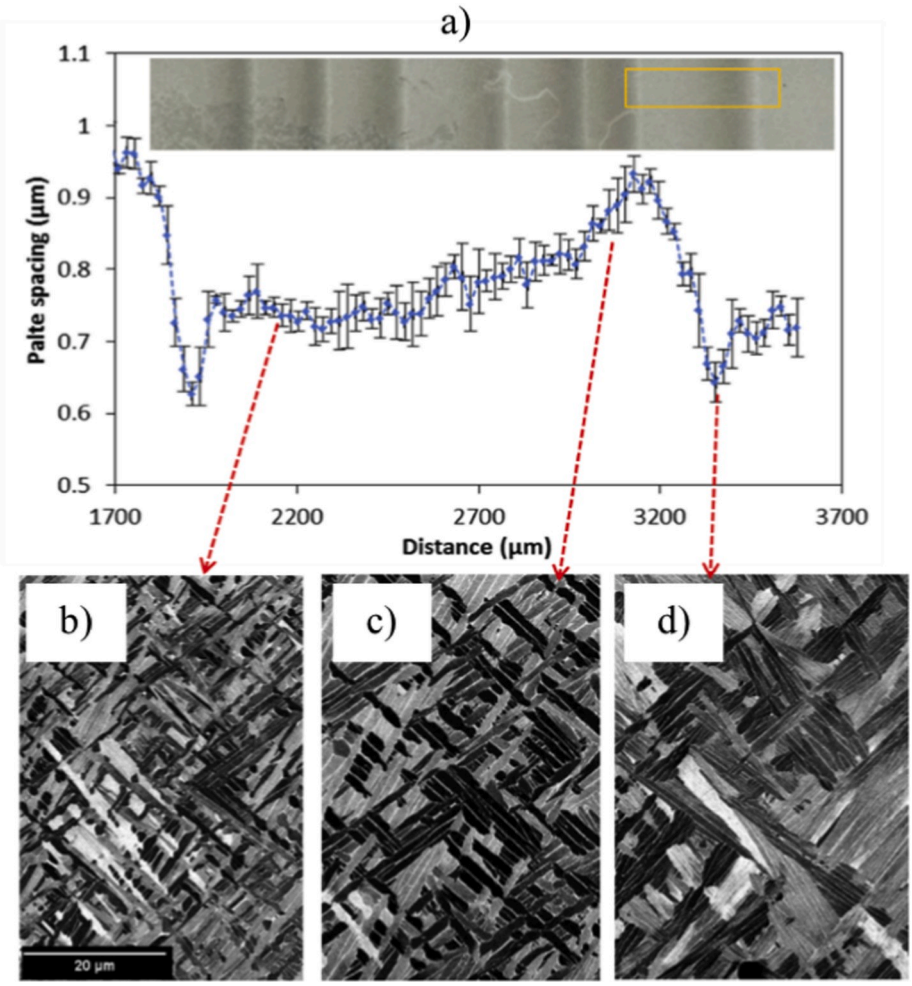

Fig. 4. Summary of the typical transformation microstructure seen in a WAAM wall across a HAZ band; (a) a graph showing the variation in α lamellae plate spacing; (b)–(d) example images of the basket weave multi-variant lamellar α microstructure seen, (b) between the HAZ bands, (c) the coarsened basket weave α within a HAZ band and (d) the thin 'white-etched layer', comprised of a finer, single-variant α colony microstructure found at the top of each HAZ band.

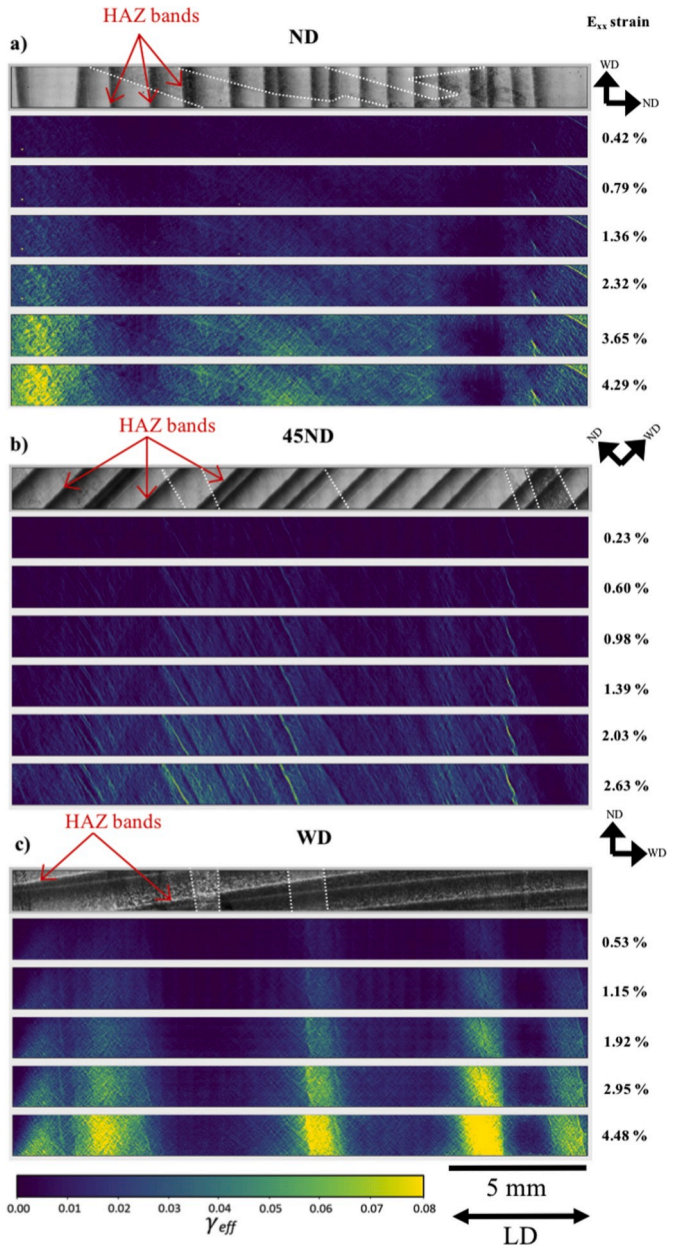

Fig. 5. Optical image maps obtained before and after tensile straining, compared to full-field surface DIC strain maps with increasing increments of sample strain, for; a) the ND, b) 45ND and c) WD sample orientations. The corresponding ε_{xx} strain values are represented on the right-hand side of each strain map (note the applied strain increments are lower for the 45ND sample, as samples with this test orientation failed at low applied strains (<4%). The HAZ bands have been indicated with red arrows; the β GBs are ~ perpendicular to the HAZ bands and can be seen form the variation in grey scale. Some β GBs have been highlighted with white dashed lines. (For interpretation of the references to colour in this figure legend, the reader is referred to the Web version of this article.)

3.2. Optical strain mapping

Interrupted tensile tests with optical DIC measurements were performed on the ND, 45ND and WD samples to compare their full-field strain localisation behaviour at increasing levels of applied strain. The tests were interrupted at strain increments of ~ 0.5% to enable optical micrograph maps of their full gauge area to be collected for DIC analysis. The average yield and maximum tensile strengths obtained for each sample orientation are summarised in Table 2. Elongations at failure are not shown as the tests were stopped early, so that post-deformation EBSD analysis could be performed to allow their strain distributions to be correlated to their microtexture. It should also be noted that due to the non-standard flat geometry of the DIC specimens, and interrupted nature of the tests, the tensile results reported are not directly comparable with those obtained from a standard tensile test. Nevertheless, the average strength levels recorded were similar to previously published data using ASTM-compatible tensile test results [26]. The results also show the opposite trend in comparison with previous work by Martina et al. [58], in that here the WD samples exhibited slightly lower σ_y and σ_{max} values than when loaded in the ND orientation. This is essentially a result of the relatively few parent ß grains present within the gauge section in the ND sample, which has skewed the results. It can also be seen that the 45ND sample exhibited the highest yield strength, which is again a texture related effect, but as discussed later, the elongation to failure for this orientation is likely to be lower than for the two other conditions.

Table 2
Mechanical properties recorded for each loading direction with the miniature DIC test samples.

	σ_y (MPa)	σ_{max} (MPa)
WD condition	763	809
45ND condition	850	906
ND condition	787	852

Optical resolution effective shear strain maps are presented in Fig. 5 for the three test orientations, with progressively increasing increments of applied plastic strain. In Fig. 5 the strain maps have been related to the underlying microstructure of each sample, captured by optical microscopy, before and after each test. It should be noted that these strain maps had an approximate pixel resolution of 17 μm and were not able to discriminate individual slip bands, but rather regions of high slip activity. Graphs showing the γ_{eff}, strain accumulation profiles obtained from these maps, along each sample's gauge length, are displayed in Fig. 6. These strain profiles have been plotted in terms of the average strain (Fig. 6a) and the 95th percentile (Fig. 6b) values, taken from each transverse row of pixels (in the sample width direction) within the data sets. The individual coloured curves correspond to each incremental increase in sample strain ($\Delta\varepsilon \approx 0.5\%$) during the DIC experiments. The 95th percentile values were chosen to highlight the comparative maximum levels of strain localisation found in each sample, at this resolution, which would otherwise be smeared out if an average value is taken when a concentrated strain band is present that is not aligned with the sample width direction (i.e. if it is at an inclined angle). The 95th percentile has been used rather than the maximum values to avoid excessive noise that would otherwise arise from taking extreme values in the data.

3.3. The ND orientation

In the ND sample, which was strained normal to the deposited layers, (Fig. 5a), the columnar grains were tilted about 10–15° from the sample's tensile axis, and the HAZ bands were transverse to the loading direction. In this specimen, apart from a concentrated single strain band appearing at the right-hand end of the gauge length, the strain distribution remained relatively homogeneous across the majority of the gauge length, until sample strains as high as 1.5% were reached and there appeared to be little correlation to the underlying microstructure. The one localised shear band that could, however, be correlated was related to the presence of a rare parent β-grain boundary orientated off axis at about 40° at the right hand end of the sample. At higher applied strains, more obvious macroscale strain patterning developed, but this still remained very diffuse with slightly more concentrated regions being seen only at the left-hand side of the sample near the gips and at its centre. At high applied strain levels, the parent β columnar grain

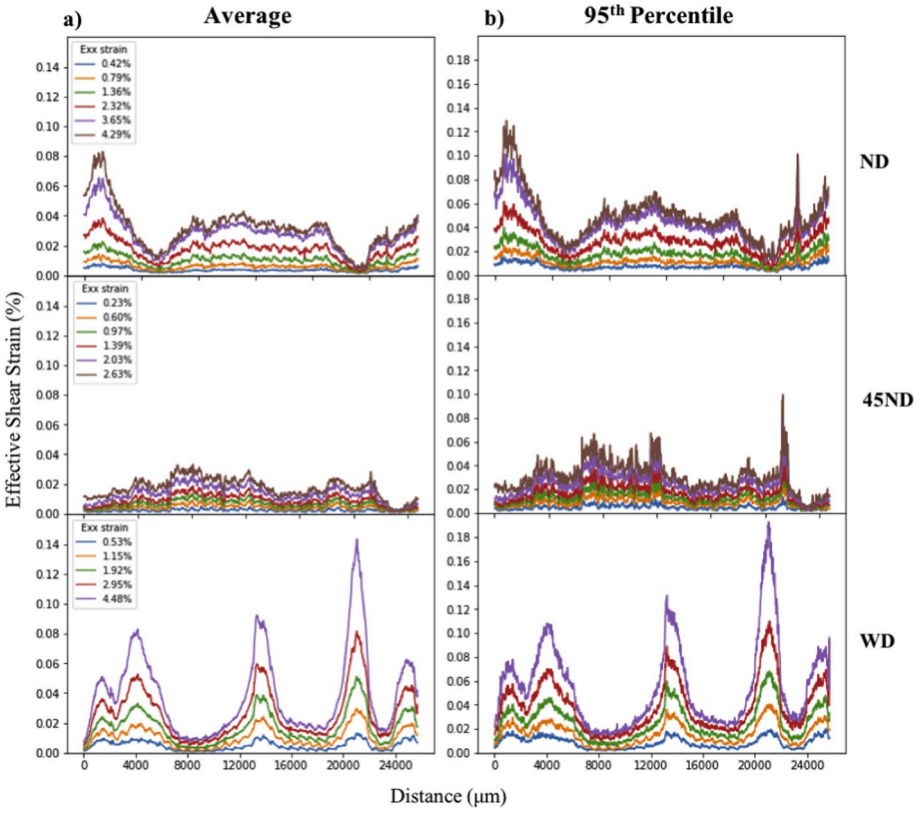

Fig. 6. - Development of effective shear strain, γ_{eff}, profiles along the samples gauge lengths with applied strain, obtained from the DIC data, averaged in the width direction, for the different sample orientations during tensile testing, showing: (a) the average and (b) 95th percentile of the effective shear strain (γ_{eff}) at each load increment. The sample strain in the loading direction is indicated in the legend. (Note the applied strain increments were slightly lower for the 45ND sample).

structure could be seen to emerge within the strain pattern, due to small differences developing in the local strains across the β GBs. The strain profiles along the gauge length (averaged in the sample width direction) provided in Fig. 6 also show relatively homogeneous flat profiles at lower strains and the maxima that built up can be seen to be broadly distributed and only reached about 2–3 times the average sample strain.

3.4. The 45ND orientation

In the 45ND specimen (Fig. 5b) the GBs were aligned around '-' 45–55° and the HAZ bands '+' ~ 45°, relative to the sample's tensile axis. In this sample a set of highly concentrated strain bands emerged even after the first applied strain increment of only 0.2%. Severe shear bands can also be seen in the final image map in Fig. 5b. These shear bands all had an angle of '-' 45 to 60° to the tensile axis and could be correlated directly with ß grain boundaries within the manufactured wall, as can be seen from comparison with the optical images (where the stronger etching HAZ bands are more obvious than the β grain boundaries). Importantly, it should be noted that such highly-localised deformation bands did not develop at all the ß GBs in the sample and, in fact, some boundaries exhibited little preferential deformation. In addition, at this resolution no mesoscale slip concentration was seen within the HAZ bands (i.e. there is no '+' 45° strain banding in Fig. 5b). This behaviour, therefore, suggests that the local microstructure associated with a specific subset of ß GBs was able to deform more easily than the grain matrices, or the HAZ bands, which were also orientated preferentially for shear in this sample (i.e. at '+' 45°). In the corresponding strain profiles depicted in Fig. 6 it can be seen that for this sample the 95th percentile taken form the data is more revealing than simply averaging in the sample width direction, as this tended to smear out the narrow strain bands because they were not aligned with the width direction. For example, the highly localised strain bands present at the ß grain boundaries in the 45ND sample and at the rare off axis GB in the ND sample are lost in the averaged data, giving a false impression that the strain is more homogeneous. In the 95th percentile plots in Fig. 6b, these narrow strain bands exhibit strain concentrations comparable with those observed in the more diffuse bands present in the WD condition, although the 45ND test was interupted at a lower applied strain of 2.5% due to fears of premature sample failure. It should also be noted that for these narrow shear bands the peak strain level recorded by optical DIC was only 1 pixel wide and was therefore concentrated in a region below the resolution limit of the optical DIC technique, and is therefore higher than could be measured at this resolution. This will be explored further below when the higher resolution data is presented.

3.5. The WD orientation

The WD tests (Fig. 5c) were performed with the samples tensile axis aligned normal to the long grain boundaries of the columnar β grains, which meant that the samples were machined out with a tilt of 15° to WD and relative to the HAZ bands, which were not expected to strongly influence the yield behaviour in this sample orientation. With the WD sample wide diffuse transverse bands, showing a higher strain concentration, developed from low applied strains (Fig. 5c). Strain localisation occurred relatively homogenously within these broad diffuse bands, which correlated with the width of certain parent ß grains, rather than in the much sharper shear bands seen in the 45ND sample. Furthermore, in this sample the strain did not appear to concentrate at the β grain boundaries, as was expected from reviewing claims made in the literature on the fracture behaviour seen on transverse loading in AM deposits [26]. In contrast, the strain distribution was found to be generally higher across the entire width of specific β grains. This behaviour can be observed by comparing the strain profiles presented in Fig. 6 with the optical micrographs and strain maps in Fig. 5c. For example, it can be

seen that the central, broad, high strain band present in Fig. 5c aligns closely with a less etched (whiter) ß grain seen in the middle of the sample and within the strain profiles in Fig. 6 the peak is centred within the grain, rather than at its boundaries. In addition, the strain within this particular β grain is significantly higher than the neighbouring grains and this higher concentration appears to interrupt at the boundary and either stop or become more diffuse. In the WD sample strain profiles shown in Fig. 6 it can also be observed that the pattern of strain localisation developed strongly from the very first straining step, with clear peaks and troughs already apparent in the first strain profile. On increasing the deformation this initial pattern simply increased in amplitude to give maximum values of more than 5 times the sample strain at the highest applied strain of 4.5%.

The above observations are supported in Fig. 7 by plotting frequency distributions of the effective shear strains measured at each pixel location across the samples' entire gauge lengths. In these plots, the effective shear strain values have been normalised by the average applied strain, due to there being slight differences in the applied strain levels between the 3 sample orientations at a particular strain increment, which ranged from 1.9 - 2.3%. Fig. 7 again demonstrates that the ND sample underwent the most uniform deformation and exhibited significantly less strain localisation than the other two test orientations, having overall the narrowest distribution and lowest maximum normalised shear strain value of 4, compared to 4.4 for the WD sample and over 5 for the 45ND test orientation. In comparison, the frequency distribution for the WD sample was broader than that for the ND test orientation, due to the presence of a shoulder in the frequency distribution at higher strain values that then rapidly declined. This shoulder reflects the broader bands of relatively uniform higher strain concertation seen in this sample. In contrast, the 45ND sample's distribution was narrower at its half maximum peak height, but had a longer tail at high strains, which is again consistent with strain becoming concentrated in narrow shear bands in this sample.

Finally, when observed at this resolution, in all of the conditions examined no influence of the HAZ bands on the strain patterning was observed. This is particularly surprising for the 45ND sample orientation

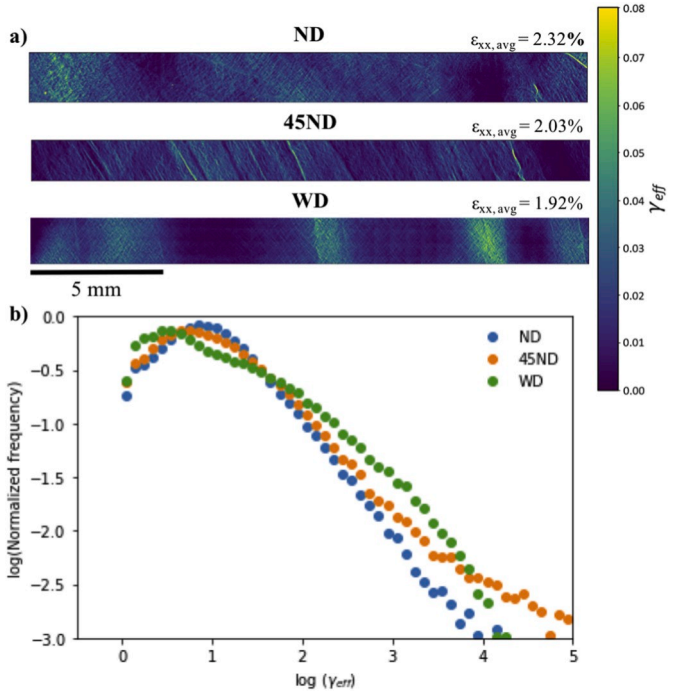

Fig. 7. Comparison of normalised frequency distributions obtained from the DIC γ_{eff} data sets, measured at each pixel location across the whole gauge length, for each sample orientation at an applied sample tensile strain of ~2%.

because the coarser transformation microstructure present within the HAZ bands (Fig. 4) might be expected to promote preferential slip, when the HAZ bands are aligned ideally for shear deformation [56].

3.6. Correlation to the microtexture

In order to better understand the origin of the regions displaying strain localisation in the strain maps presented above, their local slip behaviour has been investigated by correlating the strain data directly to the local microtexture, using EBSD orientation mapping of the same sample areas performed after deformation. To obtain the EBSD maps, regions of interest were first marked with hardness indents and then the samples were lightly re-polished to remove the etched speckle pattern. The EBSD orientation data was then used to compute α phase prismatic and basal Schmid factors for each map. The Schmid factor is the ratio of the applied stress to the component of shear stress on the corresponding slip system [59] and was calculated here following the conventional approach of using the global stress condition. This assumes that the stress state within individual α grains can be directly related to the nominal applied stress [60,61], which is not necessarily correct on the microscale as other factors, such as constraint by neighbouring variants, affect the local stress state. However, despite this approximation, when actual slip systems have been determined by TEM analysis strong agreement has generally been found between the Schmid factor predicted and actual active slip system in HCP metals [62]. In the analysis below, the pyramidal slip mode has not been considered due to the higher critical resolved shear stress (CRSS) required for its activation at room temperature [63]. Results have only been presented for the 45ND and WD sample orientations as these conditions exhibited the most intense strain localisation and provided interesting examples of both diffuse and severe strain concentration.

In the WD condition, strain localisation was found to be predominantly spread across certain parent ß grains, rather than being locally concentrated at grain boundaries as has been previously claimed [26]. In Fig. 8, a magnified effective shear strain map (Fig. 8a) has been correlated with the underlying micro-texture for an individual set of neighbouring ß grains, taken from the centre of the ND sample, that exhibited regions of high and low local strain. In the α-IPF orientation map, depicted in Fig. 8b, the different parent β grains (determined by reconstruction) have been labelled R1 - R4. At first inspection the colouration suggests that regions R1 and R3 and regions R2 and R4 might contain similar sets of α variant orientations, however, different parent β grain orientations can be clearly seen in the corresponding reconstructed β map in Fig. 8c. In this example, the DIC effective shear strain map indicated that strain concentration predominantly occurred in grain R3. Prismatic and basal Schmid factor maps (Fig. 8d and e) and their frequency distributions (Fig. 9a) have been calculated from the α orientation data for the individual β grains in Fig. 8a and are compared in Fig. 9a. This analysis shows that grains R2 and R4, neighbouring the region R3 that exhibited the highest level of deformation, had similar Schmid factor distributions, with a combination of both soft and hard α variants present for each slip mode in each grain. However, despite R1 and R3 appearing to have similar colouration in the α-IPF orientation map, grain R3 contained fewer α variants (3 as opposed to 5). Both grains had variants suitably aligned for prismatic and basal slip, but grain R1 also contained a significant fraction of α variants with a low Schmid factor for prismatic slip, which would explain the lack of deformation in this region. In contrast, grain R3 did not contain any α variants hard oriented for prismatic slip and very few for basal slip. It can also be seen in the associated pole figures (Fig. 9b) along with the subsequent misorientation line profile analysis (Fig. 9c) that misorientations greater than 15° are observed at the boundaries between grains R2 to R3 and R3 to R4, and this is smaller than the misorientation observed between grains R1 and R2. It thus appears that the underlying orientation of the local α variants present, relative to the loading direction, is of greater significance than parent β grain to grain

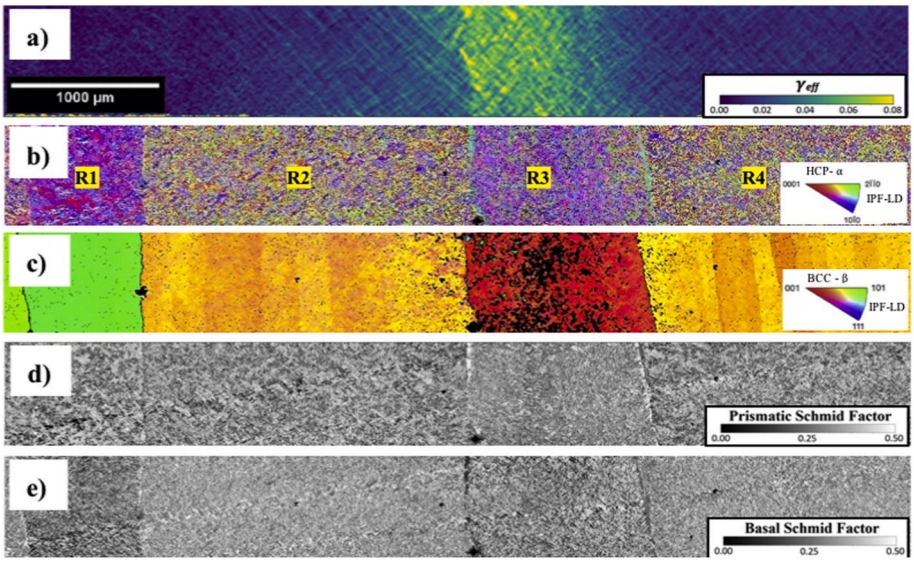

Fig. 8. Comparison of the diffuse strain localisation seen in the WD sample orientation with its underlying microtexture: (a) the effective shear strain map; (b)–(e) EBSD orientation data showing (b) an α-IPF LD map, (c) a reconstructed ß-IPF LD map, (d) prismatic and (e) basal Schmid factor maps.

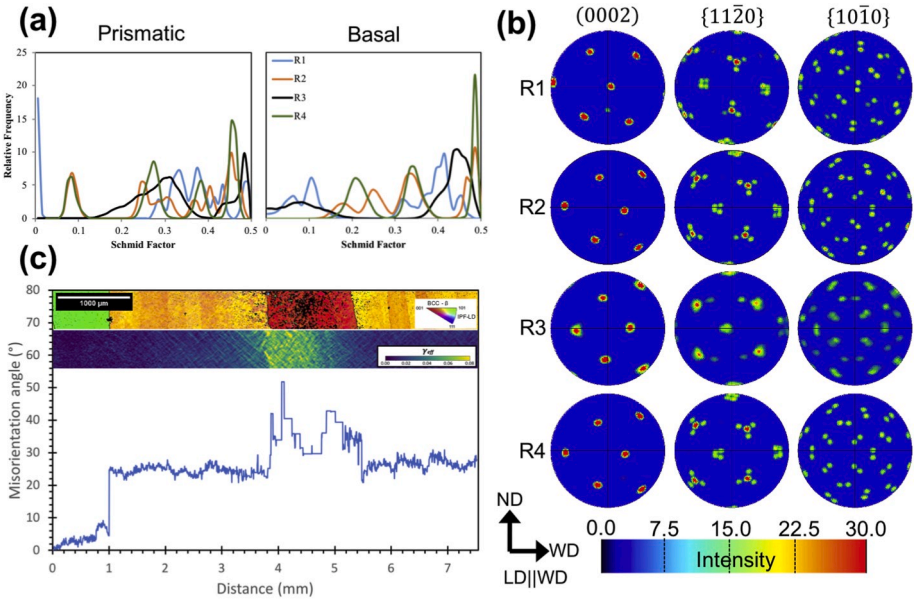

Fig. 9. - Detailed analysis of the orientation data showing; (a) distributions of prismatic and basal Schmid factors in the β-grain regions marked R1 -R4 and (b) their corresponding α-phase {0002}, {11$\bar{2}$0} and {10$\bar{1}$0} pole figures, along with (c) a misorientation profile across the ß-IPF LD map, shown with its corresponding effective shear strain map. The intensity of the pole figures means multiples of random distribution (MRD) with the pole figure orientations signified from the coordinate system.

misorientations. Overall, the Schmid factor analysis therefore shows that although all the β grains contained α variants favourably orientated for slip, the parent β grain R3, that was observed to experience the greatest strain concentration, contained the lowest proportion of α variants with a low Schmid factor: i.e. it had a *lack* of α variants able to inhibit slip, relative to its neighbouring grains that all contained some harder variants, which caused slip concentration in this grain rather than this occurring just due to there being more softer variants present locally.

On straining the 45ND sample orientation, pronounced high-strain sharp shear bands developed across the gauge length (Figs. 5–6) that were noted to be close to the positions of β grain boundaries in the optical images. In Fig. 10 an example is provided where a similar micro-texture analysis has been performed to that above, focussing on a typical high strain grain boundary region. The α phase EBSD data (Fig. 10a) and reconstructed ß phase (Fig. 10b) IPF maps show the location of the ß grain boundary, and confirms there is a distinctly different orientation across the GB region. A micro-texture layer can also be seen in the α map of the GB region, which is dominated by one colour (lilac) which is indicative of the presence of a single variant α colony microstructure, as shown in Fig. 3. By correlating the EBSD maps with the optical image after deformation (Fig. 10c) and the effective shear strain map in Fig. 10d, it can be observed that the intense strain localisation occurs near to the interface between the two parent ß grains, within the GB colony layer. Similarly, to before, the orientation map has been sub-divided into three regions; defined as R1, R2 and R3 (labelled on Fig. 10a), where R1 and R3 are the parent ß grains, either side of the high strain band, and R2 is from the high strain band itself. Schmid factor distributions for prismatic and basal slip for each region are provided in Fig. 10e and f. This shows that all 3 regions have similar distributions, with respect to the positions of the peaks in their Schmid factor distributions that result from their different α variants. This is partly caused by the fact that there is α plate inter-penetration between the colony layer and basket weave grain matrix microstructures that is

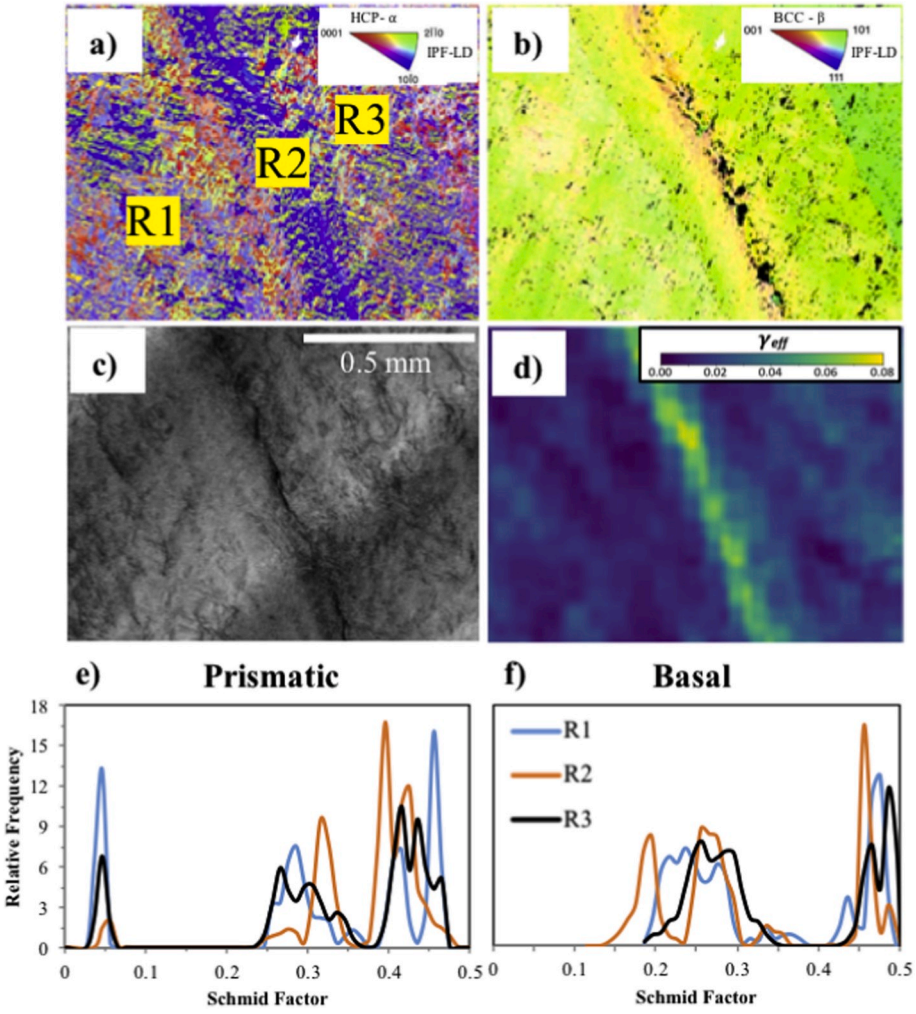

Fig. 10. - Comparison of strain localisation near a β GB to the underlying micro-texture for the 45ND sample orientation. The micros-textures determined from EBSD orientation data are presented in terms of; (a) an α-IPF LD map and (b) ß-IPF LD map, and (c) an optical image of the deformed sample with, d) the corresponding effective shear strain map. Frequency distributions of Schmid factors in the regions marked R1 - R3 (a) are shown in (e) for prismatic and (f) basal slip.

difficult to separate at this strain resolution (see Fig. 11 for high-resolution images of the microstructure captured by orientation mapping). However, significant differences in the intensities of the distributions can be seen between the GB and grain matrix regions. In particular, the GB colony region R2 has one dominant α variant (Fig. 10 e -f), whereas the grain matrix regions R1 and R3 both contain more equally represented multiple variants In addition, the GB colony region has a higher proportion of α variants with high Schmid factors that are favourably oriented for both prismatic and basal slip, whereas in the surrounding grains a much more significant fraction of α variants are 'hard' with respect to prismatic slip; meaning that in this deformation mode the GB region it is effectively acting as a soft shear layer constrained between two neighbouring harder regions. It should be noted that at this resolution, the strain localisation appears as a single band of high strain covering the entire grain boundary area and cannot be differentiated into individual slip bands, or clearly correlated to the near-GB microstructure.

3.7. *Factors affecting strain heterogeneity in WAAM microstructures*

Although slip occurs at the atomic scale, the work presented above has focused on characterizing the relationship between the coarse-scale heterogeneities commonly found in titanium material produced by high deposition rate AM and their mesoscale slip localisation, because of its importance in explaining the anisotropy commonly found in their failure behaviour (e.g. Refs. [10,14,15,26,38,58,64]). Similar research on conventional wrought titanium alloys has highlighted the influence of texture heterogeneity, such as that created by macrozones, on strain localisation [51]. For example, studies performed on Ti–6Al–4V, with an equiaxed recrystallized α microstructure have, observed crack formation during fatigue and dwell fatigue loading where coarse texture regions preferentially oriented for slip are constrained by neighbouring unfavourably oriented grains [50]. This suggests that in general a microstructure containing combinations of 'soft' and 'hard' oriented macroscopic regions, will lead to premature fracture and a greater scatter in mechanical properties.

The literature on the anisotropic behaviour of AM Ti–6Al–4V is not yet as well established, but to date there are two main conclusions. Firstly, many studies [14,33,52] have observed anisotropy in the strain to failure in tensile tests performed with respect to the build and transverse loading directions. Most of these studies have linked this behaviour to the presence of a soft grain boundary α region along the parent ß grain boundaries [20,26,33,34,37,40]. However, it is unclear if this occurs at the allotriomorphic grain boundary α, or within the associated α colonies that grow out from the GB α. Secondly, anisotropy has been observed in relation to the yield stress and related to the loading direction relative to the preferential α crystallographic texture in AM deposits [33,38]. In the results presented here, which were obtained from WAAM materials with coarse β columnar grain structures, the local texture and Schmid factor analysis has shown that the

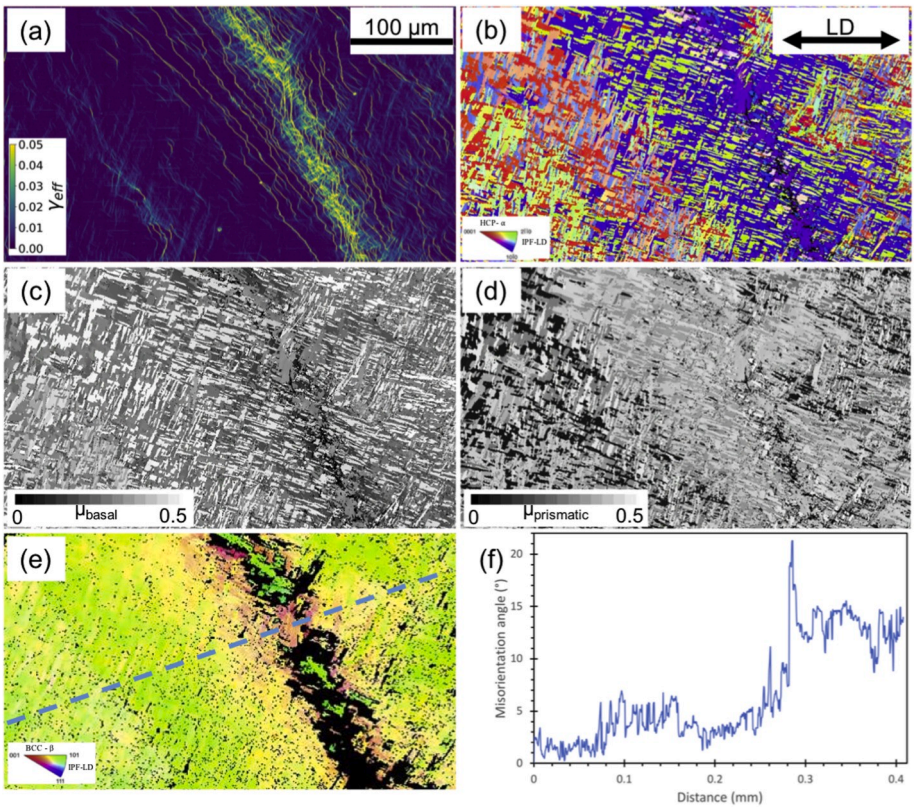

Fig. 11. High-resolution DIC analysis of the high strain GB band highlighted by optical DIC in Fig. 10, after an extra ~ 1% deformation, showing; (a) a high-resolution effective shear strain map compared to corresponding EBSD orientation data; (b) an α-IPF LD map, (c) and (d) basal and prismatic Schmid factor maps, (e) a ß phase reconstructed IPF-LD map and (f) the β phase misorientation profile across the line shown in (e).

orientation of the strain axis, with respect to the ß grain boundary plane, is not the only important consideration - rather it is this in combination with the crystallographic orientation of the individual α variants present within a parent ß grain that controls the strain heterogeneity. This is because the parent ß grain will determine the orientations of the α variants that form during the ß → α phase transformation, by the Burgers orientation relationship (BOR), which ultimately determines the slip systems of the α variants that become activated within a given volume of material and its neighbouring orientations, with which it must interact, in response to a given stress state. On loading parallel to the ND direction, the DIC samples therefore showed a relatively homogeneous strain distribution, because with this orientation there was a lack of hard-soft domains connected across the sample gauge length to interact and cause strain localisation. Loading in the ND direction therefore leads to a high strain to failure, as has been observed previously [26]. This is expected, as epitaxial ß growth during solidification of multiple layers resulted in coarse columnar ß grains aligned along the sample axis with a <001> fibre texture. On transformation to α this produces a set of similar multiple α variants within the basket weave morphology along the build height direction; i.e. in the WD sample orientation there were few abrupt boundaries between regions continuous on the scale of the sample thickness with different sets of dominant α variants along the sample gauge length. Although an occasional, unfavourably oriented GBs will exist, with respect to this loading direction, as was noted in the small tensile sample tested in Fig. 5a, such a rare event will not form a load path through a bulk material, or dramatically affect the strain to failure of larger cross-section test pieces.

Conversely, in the WD loading orientation, the loading axis was normal to the prior β columnar grain structure, with the grains being large enough to cross the entire sample's gauge width and through thickness. This gave rise to abrupt changes in the α variant orientations inhered form the β grains crossing from one grain to the next, along the gauge length. In this loading orientation the β GB plane and GB α, and its related colony layer, were approximately normal to the loading direction at the sample surfae. However, slip was not found to be concentrated specifically in the β GB regions, rather it was dispersed across soft β grains, which diverged from 'hard' grains in their strain accumulation with increasing sample deformation. This suggests that when the deformation axis is normal to a β grain boundary plane the thin GB colony structure is too constrained to enable slip to concentrate specifically in this region. Certain β grains will, however, on average contain less hard α variant orientations and still concentrate slip. This behaviour will still cause greater strain discontinuity at transverse boundaries that will lead to earlier initiation of fracture in tensile loading; i.e. when necking occurs void nucleation will be favoured at the discontinuity associated with the GB colony region, as has been suggested by previous authors [1,33]. However, probably more important in causing premature failure in larger standard tensile tests, performed on AM materials, in the transverse direction is that, although the GBs appear normal to the stress axis at the sample surface, through the thickness, with a larger sample cross section, the β grains boundary planes will vary in inclination with depth. In WD samples failure will then be more likely to occur on an inter-connected pathway of the inclined boundary planes present in the tensile sample thickness direction, by the same process of intense inter-granular shear that was seen in the 45ND loading condition.

The slip behaviour within the basket weave structures seen within the grains themselves is complex owing to the presence of multiple interwoven variants. For example, Banerjee has shown that slip transfer between variants is possible in some tri-variant colonies, which then act collectively as a 'grain' in terms of their slip line length [65]. Here, we have not yet resolved the specific traces within the β grain matrix as the optical DIC was too low resolution to distinguish individual slip bands. We have, however, found a direct correlation between the concentration of deformation in multi-variant (basket weave) regions where there is an

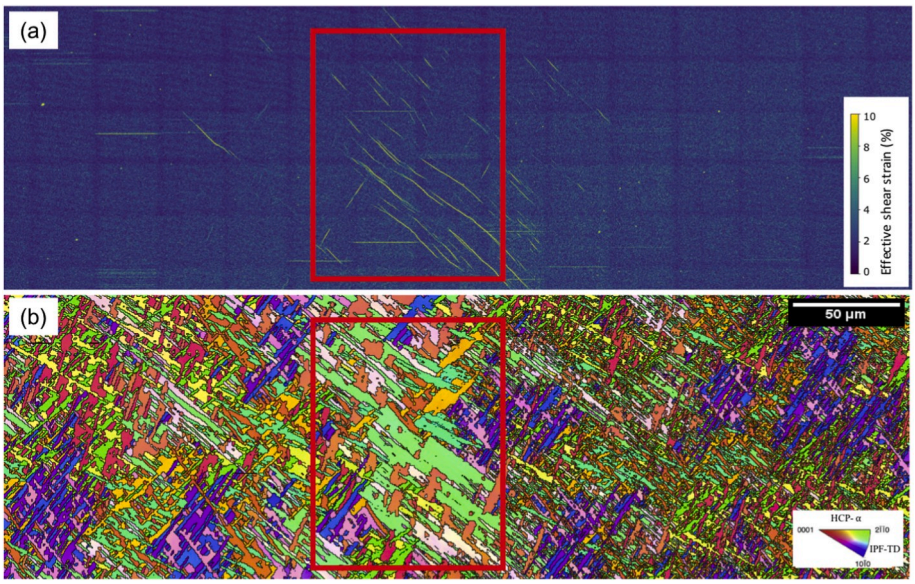

Fig. 12. High-resolution DIC performed across a HAZ band loaded parallel to ND, to below the yield point ($0.8\sigma_y$) showing; (a) the effective shear strain map and (b) a corresponding EBSD inverse pole figure (IPF-TD) map depicting the morphology and crystal orientation of the α phase. Note; the micro-strain occurring parallel to the α lamellar in the coarser single-variant colonies seen at the top of the HAZ band.

absence of any 'hard' α variants with low Schmid factors for prismatic or basal slip. This occurs because there are typically at least three α variants present, and at least one or two of these are always reasonably favourably orientated for active slip. However, it is rarer that all three variants are simultaneously found to have high Schmid factors for basal or prismatic slip. In the results above, despite the limitations of calculating the Schmid factor based on the sample loading direction, this condition - where there was a lack of a single hard variant orientation in a region - always coincided with where a high local strain was detected in the DIC results.

In the 45ND sample, which was loaded at 45° to the build direction, very highly localised shear bands were seen in the vicinity of the columnar ß grain boundaries. It is therefore of concern that little mechanical test data is currently published in the literature for coarse grained AM materials loaded off-axis to their build normal or transverse directions. Because the optical DIC was unable to resolve the exact location of slip localisation in relation to the GB colony microstructure, the slip behaviour at the GB shown in the 45ND sample in Fig. 10 has been further investigated at a higher resolution, after a further ~1% sample strain was applied in the loading direction. In addition, Fig. 11, is presented to more clearly compare the resultant high-resolution shear strain map from this region with the corresponding local mircrotexture. From Fig. 11a, it can be observed that long, slip bands can now be resolved parallel to ND, where many of these slip bands propagate across multiple α lath boundaries showing that the ß in between the laths has little effect on the slip transfer across them [54]. There is also an intense broader transgranular band of strain close to the GB. Slip on either side of the GB occurs in multiple individual slip bands that are spread out into the matrix over a distance of ~ 20–50 μm. However, within the colony α GB layer there is a wider intense band of strain along the entire GB region. This deformation band also shows evidence of short individual slip bands that are perpendicular to the GB, within individual α laths. The width of the intense strain band is ~ 30 μm, which is equal to the typical width of an α GB colony layer found in the WAAM material (Fig. 3). The basal and prismatic Schmid factor maps, Fig. 11c and d, show that in the colony region along the GB the dominant α variant present is favourably oriented for both basal and prismatic slip systems. However, the misorientation profile across the reconstructed ß IPF map, Fig. 11e, shows a misorientation of only ~ 10° between the two β grains. This higher resolution strain map has thus enabled the strain discontinuity at the GB to be further examined and indicates that, in this case, the α GB colony layer consisted of a dominant α variant with a soft orientation, which led to an intense band of slip equal to its width developing across the GB, despite the misorientation between the two neighbouring ß grains being relatively low.

Finally, at the mesoscale, in the strain distributions presented above the HAZ bands which appear as strongly etching microstructure heterogeneities in WAAM deposits (Figs. 2a & 4) were found to exhibit little influence on the strain localisation, even when orientated at 45° to the load axis when they would be perfectly orientated for shear. This is despite the transformation microstructure within the HAZ bands having coarsened to form a local layer with 'softer' basket weave α lamellar, as well as the top of each HAZ band terminating with a thin layer of colony α (Fig. 4). In a previous study by Foehring et al. [34] that also used DIC to investigate the tensile behaviour in AM Ti–6Al–4V, it was reported that strain could preferentially accumulate along the interfaces between consecutive deposited layer bands; however, this has not been observed here. Detailed measurement of the α spacing across multiple HAZ bands by Ho et al. in similar WAAM deposits [15] has shown that in the steady state part of walls the α lamellar spacing typically increases from an average of ~ 0.8 μm to ~ 1 μm (Fig. 4). According to the Hall-Petch relationship fitted to the α lath lamellar spacing [66], this would only result in a yield strength reduction of less than 3%, which is therefore probably insignificant relative to the stronger effect of microtexture on yielding in Ti–6Al–4V.

To investigate this further, HRDIC has been performed on a typical HAZ band loaded in the ND orientation to low applied strains, just below the materials yield stress (~80% $\sigma_{0.2}$). The results in Fig. 12 show that in this sample micro-slip initiated within the colony layer in the HAZ band, but not in the layer with the coarsened basket weave microstructure, despite the load not having exceeded the materials bulk yield stress. In the colony layer, it can be seen in Fig. 12b that there is a greater effective α 'grain size' due to the presence of larger domains with a single α variant. The HAZ band region shown by the red box in Fig. 12 has been analysed further in Fig. 13. From the data in Fig. 13, it can be seen that in this particular α colony highly localised slip has occurred, parallel to the lamellar, which are favourably geometrically aligned at 45° to the tensile axis. In addition, the particular α variant that has under gone local micro-slip also has a high Schmid factor for basal slip, but a low Schmid factor for prismatic slip. The CRSS for basal and prismatic slip are very

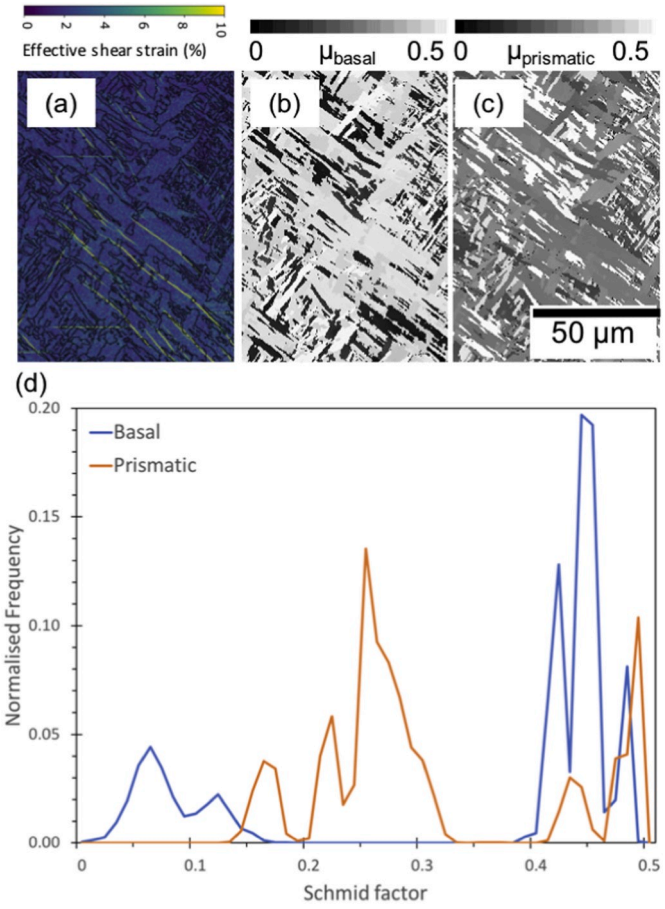

Fig. 13. - Analysis of the slip systems operating in the HAZ band region, shown in Fig. 12, comparing in (a) the effective local shear strain to (b) prismatic and (c) basal Schmid factor maps, with the distributions of the prismatic and basal Schmid factors provided in (d).

close in Ti–6Al–4V and the dominance of basal slip at lower stress levels has also been observed in previous studies on titanium alloys when it favoured by the plate geometry [67,68]. However, this micro-deformation that was observed locally in the colony layer was not found to extend to create a mesoscale bands of slip concentration that would be visible at lower resolution in the optical full sample-field DIC results shown above. This is probably because, in contrast to the α colonies seen at β GBs, the HAZ colony layer is not comprised of one continuous orientation, but changes locally and is interpenetrated by other variants. This would prevent it spreading to form a continuous deformation band along a HAZ layer and micro-yielding was thus only seen locally where there is a highly favourable set of circumstances (i.e. where there is a colony that coincidently has its lath long-axis and a favourable slip system both aligned with the shear plane). In addition, at a β GB there is normally a far higher texture discontinuity, created by the grain matrix α variants inherited from the different parent β grains either side of the boundary. Although not as significant in a tensile test, these higher resolution DIC observations do, though, suggest that the presence of micro-yielding in HAZ band at mechanical loads below the yield point could be important for high cycle fatigue performance.

4. Conclusions

The significance of the microstructure and texture heterogeneity apparent in samples manufactured by high deposition rate AM processes, with a Ti–6Al–4V alloy, on strain localisation, has been investigated using both full-field optical mesoscale and high-resolution microscale strain mapping, by correlating results obtained by digital image correlation to the underlying micro-texture. The investigation was performed on single deposition track wide WAAM samples, tested in tension at three different orientations relative to the build direction; normal to the deposited layers (ND), perpendicular to the columnar grains (WD) and at 45° to the build direction (45ND). The results have been correlated to EBSD orientation maps, to relate the strain behaviour to the approximate Schmid factors of the α variants present within the transformation microstructure in different regions of the material. The main conclusions are as follows:

- Deformation was relatively homogeneous in the ND sample orientation, as the majority of the α variants present in the specimen were transformed from a single ß grain along the gauge length, and there were therefore few abrupt discontinuities formed by ß grain boundaries. In contrast, the strain distributions in the 45ND and WD (horizontal) orientations were highly heterogeneous and resulted in severe strain concentration.
- Regions of high strain in the transverse WD condition were relatively diffuse and could be correlated to 'softer' ß grains that contained an absence of harder α variant orientations. Whereas; in the 45ND condition sharp, far more highly concentrated, shear bands were observed near parent ß grain boundaries. HRDIC of the GB region showed that these shear bands were confined within the GB colony microstructure and were not concentrated specifically within the GB α region.
- In both the 45ND and WD loading cases, where significant strain localisation was observed the transformation microstructure was found to be effectively softer, because it lacked α variants that had hard orientations with respect to prismatic and/or basal slip. This generally resulted in a softer region being constrained between harder neighbouring regions that contained one or more α variants with a low Schmid factor for prismatic and/or basal slip.
- From these results it can be inferred that in conventional tensile tests the premature failure that is frequently reported to occur in transverse loading occurs by shear concentration at columnar β grain boundaries, that are inclined with respect to the sample gauge length, rather than by GB rupture under tensile loading normal to the GB plane.
- In tensile deformation, the HAZ banding was shown to have little influence on the microscale strain distribution for any of the sample orientations. This has been attributed to the relatively small effect of α lamellar coarsening on the local yield response, relative to the stronger influence of microtexture in Titanium alloys. Although, HRDIC analysis showed that localised slip was possible within the HAZ bands where coarser colony regions were seen within the thin 'white' layer, even below the bulk yield point, this only occurred in local colonies favourably orientated for slip which were not continuous along the whole HAZ band.

Data availability

The raw/processed data required to reproduce these findings cannot be shared at this time due to technical or time limitations.

Declaration of competing interest

The authors declare that they have no known competing financial interests or personal relationships that could have appeared to influence the work reported in this paper.

CRediT authorship contribution statement

David Lunt: Conceptualization, Methodology, Formal analysis, Investigation, Writing - original draft, Writing - review & editing, Visualization. **Alistair Ho:** Conceptualization, Methodology, Formal analysis, Investigation, Visualization. **Alec Davis:** Investigation, Writing - review & editing. **Allan Harte:** Investigation, Formal analysis. **Filomeno Martina:** Resources. **João Quinta da Fonseca:** Writing - review & editing, Visualization, Supervision. **Philip Prangnell:** Conceptualization, Writing - review & editing, Visualization, Supervision, Project administration, Funding acquisition.

Acknowledgements

The authors are appreciative of the EPSRC (grants LightForm - EP/R001715/1; NEWAM – EP/R027218/1) and Innovate UK (Open Architecture Additive Manufacturing, OAAM) for supporting aspects of this research. P.B. Prangnell is also grateful to the Royal Academy of Engineering, UK and Airbus UK for financial support.

Appendix A. Supplementary data

Supplementary data to this article can be found online at https://doi.org/10.1016/j.msea.2020.139608.

References

[1] G. Lutjering, Influence of processing on microstructure and mechanical properties of (α+β) titanium alloys, Mater. Sci. Eng., A 243 (1–2) (Mar. 1998) 32–45.
[2] M. Peters, C. Leyens, Titanium and Titanium Alloys, 2003.
[3] E. Ezugwu, J. Bonney, Y. Yamane, An overview of the machinability of aeroengine alloys, J. Mater. Process. Technol. 134 (2) (Mar. 2003) 233–253.
[4] R. Boyer, An overview on the use of titanium in the aerospace industry, Mater. Sci. Eng., A 213 (1–2) (Aug. 1996) 103–114.
[5] W.J. Sames, F.A. List, S. Pannala, R.R. Dehoff, S.S. Babu, The metallurgy and processing science of metal additive manufacturing, Int. Mater. Rev. 61 (5) (Jul. 2016) 315–360.
[6] D. Herzog, V. Seyda, E. Wycisk, C. Emmelmann, Additive manufacturing of metals, Acta Mater. 117 (2016) 371–392.
[7] D. Bourell, et al., Materials for additive manufacturing, CIRP Ann. - Manuf. Technol. 66 (2) (2017) 659–681.
[8] T. Debroy, et al., Progress in Materials Science Additive manufacturing of metallic components – process, structure and properties, Prog. Mater. Sci. 92 (2018) 112–224.
[9] W.E. Frazier, Metal additive manufacturing: a review, J. Mater. Eng. Perform. 23 (6) (2014) 1917–1928.
[10] J.J. Lewandowski, M. Seifi, Metal additive manufacturing: a review of mechanical properties, Annu. Rev. Mater. Res. 46 (1) (Jul. 2016) 151–186.

[11] S. Liu, Y.C. Shin, Additive manufacturing of Ti6Al4V alloy: a review, Mater. Des. 164 (2018) 107552.
[12] E. Herderick, Additive manufacturing of metals: a review, Mater. Sci. Technol. Conf. Exhib. 2 (176252) (2011) 1413–1425, 2011.
[13] J.S. Keist, T.A. Palmer, Role of geometry on properties of additively manufactured Ti-6Al-4V structures fabricated using laser based directed energy deposition, Mater. Des. 106 (2016) 482–494.
[14] B.E. Carroll, T.A. Palmer, A.M. Beese, Anisotropic tensile behavior of Ti-6Al-4V components fabricated with directed energy deposition additive manufacturing, Acta Mater. 87 (2015) 309–320.
[15] A. Ho, H. Zhao, J.W. Fellowes, F. Martina, A.E. Davis, P.B. Prangnell, On the origin of microstructural banding in Ti-6Al4V wire-arc based high deposition rate additive manufacturing, Acta Mater. 166 (2019) 306–323.
[16] C. Körner, Additive manufacturing of metallic components by selective electron beam melting - a review, Int. Mater. Rev. 61 (5) (Jul. 2016) 361–377.
[17] Q. Yang, P. Zhang, L. Cheng, Z. Min, M. Chyu, A.C. To, Finite element modeling and validation of thermomechanical behavior of Ti-6Al-4V in directed energy deposition additive manufacturing, Addit. Manuf. 12 (Oct. 2016) 169–177.
[18] V.D. Fachinotti, A. Cardona, B. Baufeld, O. Van Der Biest, Finite-element modelling of heat transfer in shaped metal deposition and experimental validation, Acta Mater. 60 (19) (2012) 6621–6630.
[19] C. Charles, N. Jarvstrat, Modelling Ti-6Al-4V microstructure by evolution laws implemented as finite element subroutines: application to TIG metal deposition, Proc. 8th Int. Conf. Trends Weld. Res. (2009) 477–485.
[20] E. Brandl, B. Baufeld, C. Leyens, R. Gault, Additive manufactured Ti-6Al-4V using welding wire: comparison of laser and arc beam deposition and evaluation with respect to aerospace material specifications, Phys. Procedia 5 (2010) 595–606. PART 2.
[21] B. Baufeld, O. Van der Biest, R. Gault, "Additive manufacturing of Ti–6Al–4V components by shaped metal deposition: microstructure and mechanical properties, Mater. Des. 31 (Jun. 2010) S106–S111.
[22] F. Wang, S. Williams, M. Rush, Morphology investigation on direct current pulsed gas tungsten arc welded additive layer manufactured Ti6Al4V alloy, Int. J. Adv. Manuf. Technol. 57 (5–8) (2011) 597–603.
[23] B. Baufeld, E. Brandl, O. Van Der Biest, Wire based additive layer manufacturing: comparison of microstructure and mechanical properties of Ti-6Al-4V components fabricated by laser-beam deposition and shaped metal deposition, J. Mater. Process. Technol. 211 (6) (Jun. 2011) 1146–1158.
[24] S.H. Mok, G. Bi, J. Folkes, I. Pashby, J. Segal, "Deposition of Ti–6Al–4V using a high power diode laser and wire, Part II: investigation on the mechanical properties, Surf. Coating. Technol. 202 (19) (Jun. 2008) 4613–4619.
[25] E. Brandl, A. Schoberth, C. Leyens, Morphology, microstructure, and hardness of titanium (Ti-6Al-4V) blocks deposited by wire-feed additive layer manufacturing (ALM), Mater. Sci. Eng., A 532 (Jan. 2012) 295–307.
[26] F. Wang, S. Williams, P. Colegrove, A.A. Antonysamy, Microstructure and mechanical properties of wire and arc additive manufactured Ti-6Al-4V, Metall. Mater. Trans. A Phys. Metall. Mater. Sci. 44 (2) (Feb. 2013) 968–977.
[27] J.J. Lin, et al., Microstructural evolution and mechanical properties of Ti-6Al-4V wall deposited by pulsed plasma arc additive manufacturing, Mater. Des. 102 (Jul. 2016) 30–40.
[28] J. Irwin, E.(Ted) Reutzel, P. Michaleris, J. Keist, A.R. Nassar, Predicting microstructure from thermal history during additive manufacturing for Ti-6Al-4V, J. Manuf. Sci. Eng. 138 (11) (2016), 111007-111007–11.
[29] G.C. Obasi, S. Birosca, J. Quinta da Fonseca, M. Preuss, "Effect of β grain growth on variant selection and texture memory effect during α→β→α phase transformation in Ti–6 Al–4 V, Acta Mater. 60 (3) (Feb. 2012) 1048–1058.
[30] D. Bhattacharyya, G.B. Viswanathan, H.L. Fraser, Crystallographic and morphological relationships between β phase and the Widmanstätten and allotriomorphic α phase at special β grain boundaries in an α/β titanium alloy, Acta Mater. 55 (20) (2007) 6765–6778.
[31] K.M. Taminger, R.A. Hafley, Electron beam freeform fabrication for cost effective near-net shape manufacturing, Spec. Meet. Cost Eff. Manuf. via Net Shape Process 16 (2006) 1–10 (NATO/RTO AVT-139).
[32] F. Martina, J. Mehnen, S.W. Williams, P. Colegrove, F. Wang, "Investigation of the benefits of plasma deposition for the additive layer manufacture of Ti–6Al–4V, J. Mater. Process. Technol. 212 (6) (Jun. 2012) 1377–1386.
[33] P. Åkerfeldt, M.-L. Antti, R. Pederson, Influence of microstructure on mechanical properties of laser metal wire-deposited Ti-6Al-4V, Mater. Sci. Eng., A 674 (2016) 428–437.
[34] D. Foehring, H.B. Chew, J. Lambros, Characterizing the tensile behavior of additively manufactured Ti-6Al-4V using multiscale digital image correlation, February, Mater. Sci. Eng., A 724 (2018) 536–546.
[35] B. Baufeld, O. Van Der Biest, S. Dillien, Texture and crystal orientation in Ti-6Al-4V builds fabricated by shaped metal deposition, Metall. Mater. Trans. A Phys. Metall. Mater. Sci. 41 (8) (2010) 1917–1927.
[36] E. Brandl, F. Palm, V. Michailov, B. Viehweger, C. Leyens, "Mechanical properties of additive manufactured titanium (Ti–6Al–4V) blocks deposited by a solid-state laser and wire, Mater. Des. 32 (10) (Dec. 2011) 4665–4675.
[37] J.S. Keist, T.A. Palmer, Role of geometry on properties of additively manufactured Ti-6Al-4V structures fabricated using laser based directed energy deposition, Mater. Des. 106 (2016) 482–494.
[38] J. Yang, H. Yu, Z. Wang, X. Zeng, Effect of crystallographic orientation on mechanical anisotropy of selective laser melted Ti-6Al-4V alloy, Mater. Char. 127 (May 2017) 137–145.
[39] P.A. Kobryn, S.L. Semiatin, Mechanical Properties of Laser-Deposited Ti-6Al-4V, 2001.
[40] M. Simonelli, Y.Y. Tse, C. Tuck, "The formation of α + β microstructure in as-fabricated selective laser melting of Ti–6Al–4V, J. Mater. Res. 29 (17) (2014) 2028–2035.
[41] J. Quinta Da Fonseca, P.M. Mummery, P.J. Withers, Full-field strain mapping by optical correlation of micrographs, J. Microsc. 218 (April) (2005) 9–21.
[42] G. Martin, C.W. Sinclair, R.A. Lebensohn, Microscale plastic strain heterogeneity in slip dominated deformation of magnesium alloy containing rare earth, Mater. Sci. Eng., A 603 (May 2014) 37–51.
[43] H.A. Padilla, J. Lambros, A.J. Beaudoin, I.M. Robertson, Relating inhomogeneous deformation to local texture in zirconium through grain-scale digital image correlation strain mapping experiments, Int. J. Solid Struct. 49 (1) (Jan. 2012) 18–31.
[44] F. Hild, S. Roux, Digital image correlation: from displacement measurement to identification of elastic properties - a Review, Strain 42 (2) (2006) 69–80.
[45] F. Gioacchino, J. Quinta da Fonseca, Plastic strain mapping with sub-micron resolution using digital image correlation, Exp. Mech. (Oct. 2012).
[46] B. Pan, K. Qian, H. Xie, A. Asundi, Two-dimensional digital image correlation for in-plane displacement and strain measurement: a review, Meas. Sci. Technol. 20 (6) (Jun. 2009), 062001.
[47] M.A. Tschopp, B.B. Bartha, W.J. Porter, P.T. Murray, S.B. Fairchild, Microstructure-dependent local strain behavior in polycrystals through in-situ scanning electron microscope tensile experiments, Metall. Mater. Trans. 40 (10) (Aug. 2009) 2363–2368.
[48] F. Hild, S. Roux, Comparison of local and global approaches to digital image correlation, Exp. Mech. (Mar. 2012) 1503–1519.
[49] J.D. Carroll, W. Abuzaid, J. Lambros, H. Sehitoglu, High resolution digital image correlation measurements of strain accumulation in fatigue crack growth, Int. J. Fatig. 57 (Dec. 2013) 140–150, https://doi.org/10.1016/j.ijfatigue.2012.06.010.
[50] P.D. Littlewood, A.J. Wilkinson, "Local deformation patterns in Ti–6Al–4V under tensile, fatigue and dwell fatigue loading, Int. J. Fatig. 43 (Oct. 2012) 111–119.
[51] D. Lunt, J. Quinta da Fonseca, D. Rugg, M. Preuss, Microscopic strain localisation in Ti-6Al-4V during uniaxial tensile loading, Mater. Sci. Eng., A 680 (680) (2017) 444–453.
[52] T.A. Book, M.D. Sangid, Materials Characterization Strain localization in Ti-6Al-4V Widmanstätten microstructures produced by additive manufacturing, Mater. Char. 122 (2016) 104–112.
[53] F. Di Gioacchino, J. Quinta Da Fonseca, An experimental study of the polycrystalline plasticity of austenitic stainless steel, Int. J. Plast. 74 (2015) 92–109.
[54] D. Lunt, X. Xu, T. Busolo, J. Quinta da Fonseca, M. Preuss, Quantification of strain localisation in a bimodal two-phase titanium alloy, Scripta Mater. 145 (2018) 45–49.
[55] P.S. Davies, B.P. Wynne, W.M. Rainforth, M.J. Thomas, P.L. Threadgill, Development of microstructure and crystallographic texture during stationary shoulder friction stir welding of Ti-6Al-4V, Metall. Mater. Trans. A Phys. Metall. Mater. Sci. 42 (8) (2011) 2278–2289.
[56] H. Zhao, A. Ho, A. Davis, A. Antonysamy, P. Prangnell, Automated Image Mapping and Quantification of Microstructure Heterogeneity in Additive Manufactured Ti6Al4V, Mater. Charact (2019).
[57] E. Lee, R. Banerjee, S. Kar, D. Bhattacharyya, H.L. Fraser, Selection of α variants during microstructural evolution in α/β titanium alloys, Philos. Mag. 87 (24) (2007) 3615–3627.
[58] F. Martina, S.W. Williams, P. Colegrove, Improved microstructure and increased mechanical properties of additive manufacture produced Ti-6Al-4V by interpass cold rolling, SFF Symp (2013) 490–496.
[59] D. Hull, D.J. Bacon, Introduction to Dislocations, vol. 37, Elsevier, 2011.
[60] F. Bridier, P. Villechaise, J. Mendez, Analysis of the different slip systems activated by tension in a alpha+beta titanium alloy in relation with local crystallographic orientation, Acta Mater. 53 (3) (Feb-2005) 555–567.
[61] H. Li, D.E. Mason, Y. Yang, T.R. Bieler, M.a. Crimp, C.J. Boehlert, "Comparison of the deformation behaviour of commercially pure titanium and Ti–5Al–2.5Sn(wt.%) at 296 and 728 K, Philos. Mag. 93 (21) (Jul. 2013) 2875–2895.
[62] X. Xu, et al., Identification of active slip mode in a hexagonal material by correlative scanning electron microscopy, Acta Mater. 175 (2019) 376–393.
[63] G. Lutjering, J.C. Williams, Titanium, second ed., 2003.
[64] J. Lu, L. Chang, J. Wang, L. Sang, S. Wu, Y. Zhang, In-situ investigation of the anisotropic mechanical properties of laser direct metal deposition Ti6Al4V alloy, Mater. Sci. Eng., A 712 (2018) 199–205. August 2017.
[65] D. Banerjee, J.C. Williams, Microstructure and slip character in titanium alloys, Defence Sci. J. 36 (2) (1986) 191–206.
[66] K. Maruyama, N. Yamada, H. Sato, Effects of lamellar spacing on mechanical properties of fully lamellar Ti - 39.4mol%Al alloy, Mater. Sci. Eng. A (2001).
[67] C. Lavogiez, S. Hémery, P. Villechaise, Analysis of deformation mechanisms operating under fatigue and dwell-fatigue loadings in an α/β titanium alloy, Int. J. Fatig. 131 (2020) 105341.
[68] S. Hémery, P. Villechaise, On the influence of ageing on the onset of plastic slip in Ti-6Al-4V at room temperature: insight on dwell fatigue behavior, Scripta Mater. 130 (2017) 157–160.

2020-05-21

The effect of loading direction on strain localisation in wire arc additively þÿ m a n u f a c t u r e d T i 6 A l 4 V

Lunt, David

Elsevier

Lunt D, Ho A, Davis A, et al., (2020) The effect of loading direction on strain localisation in wire þÿ a r c a d d i t i v e l y m a n u f a c t u r e d T i 6 A l 4 V , M a t e r i a l s S c i e n c e a n d E n g i n e e r i n Materials: Properties. Microstructures and Processing, Volume 788, June 2020, Article number 139608

https://doi.org/10.1016/j.msea.2020.139608